Journal of Materials Research and Technology 32 (2024) 2931–2944

Contents lists available at ScienceDirect

Journal of Materials Research and Technology

journal homepage: www.elsevier.com/locate/jmrt

Study of bainite and martensite tempering in a medium C high Si steel. microstructural disparities and equilibrium convergence

Mattia Franceschi [a], Lucia Morales-Rivas [b], Erick Cordova-Tapia [b], Jose A. Jimenez [b], Manuele Dabalà [c], Carlos Garcia-Mateo [b,*]

[a] Department of Engineering and Management, University of Padova, Stradella San Nicola 3, 36100, Vicenza, Italy
[b] Department of Physical Metallurgy, National Center for Metallurgical Research (CENIM-CSIC), MATERALIA Research Group, Avenida Gregorio del Amo, 8, Madrid, 28040, Spain
[c] Department of Industrial Engineering, University of Padova, Via Marzolo 9, 35131, Padova, Italy

ARTICLE INFO

Keywords:
Bainite
Martensite
Austenite
Tempering
Dilatometry
XRD

ABSTRACT

This study investigates the tempering behavior of bainite and martensite in a medium carbon, high silicon steel, with a focus on the microstructural evolution and the attainment of equilibrium, over a temperature range of 200–650 °C. The dissimilarities between the characteristics of the two initial microstructures, both comprising a C-saturated tetragonal ferrite matrix and retained austenite, are reflected in the differences observed in their evolution towards equilibrium as the tempering temperature increases. Therefore, while retained austenite plays a pivotal role in the bainitic microstructure, in the martensitic microstructure it is the ferritic matrix, which is highly dislocated and enriched in carbon, that plays a determinant role. The findings demonstrate that while both bainite and martensite can converge towards the same equilibrium state upon high-temperature tempering (600–650 °C), the pathway to this convergence is markedly different, with bainite exhibiting a slower transformation rate. This path to equilibrium has been characterised by means of high-resolution dilatometry, scanning electron microscopy and detailed X-ray diffraction analysis. This has provided a dynamic and detailed picture of the most relevant microstructural changes and tempering mechanisms in high silicon steels. It has also provided a foundation for tailoring heat treatment processes to optimise the mechanical properties of advanced bainitic and martensitic steels.

1. Introduction

It is well known that martensitic transformation in steels takes place in an adiffusional and displacive manner, resulting in a microstructure composed of a martensitic ferrite matrix and, in most cases, some retained austenite. The adiffusional character of the transformation means that both phases preserve the chemical composition of the austenite from which they originate, that of the bulk, and therefore the martensitic ferrite has a tetragonal crystallographic structure (bct) which allows it to retain in solid solution large quantities of C. The transformation also introduces a high density of dislocations due to its displacive nature [1].

It is also possible to develop bainitic microstructures, which, although also of a displacive nature, have the particularity that the C during nucleation (para-equilibrium) and after growth (adiffusional) is redistributed from the bainitic ferrite to the retained austenite surrounding it [2]. When the bainitic transformation takes place at low T, and the chemical composition contains Si sufficient to delay and even prevent cementite precipitation during the transformation, the end result is that of a matrix of bainitic ferrite, also tetragonal and supersaturated in C and retained austenite with a high C content in solid solution, which also has a high dislocation density although lower than that of martensite [2].

The reasons why it is necessary for any of these microstructures to be reheated at a certain temperature-time are various. In the case of martensite, the final microstructure is usually characterized by a high mechanical strength which is not accompanied by good ductility and toughness, thus requiring further heat thermal process, tempering to achieve required balance of strength-toughness and ductility for the final application of the steel [3,4]. It is also the case that these microstructures, bainite and martensite, work in conditions where the working temperature is higher than the ambient temperature [5]. In either

* Corresponding author. CENIM-CSIC. Avda. Gregorio del Amo 8, Madrid, 28040, Spain.
E-mail addresses: cgm@cenim.csic.es, c.g.mateo@csic.es (C. Garcia-Mateo).

https://doi.org/10.1016/j.jmrt.2024.08.141
Received 25 April 2024; Received in revised form 14 August 2024; Accepted 21 August 2024
Available online 22 August 2024

Table 1
Chemical composition of the investigated steel in wt.% and the experimentally determined Ms temperature (°C).

C	Si	Mn	Cr	Ni	Cu	Mo	Al	M_s (°C)
0.38	3.2	2.56	0.05	0.074	0.060	0.022	0.105	267

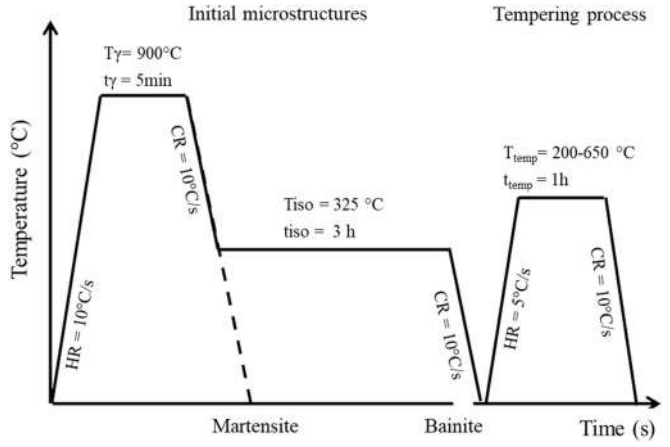

Fig. 1. Scheme of the heat treatments applied in this work to obtain the initial microstructures followed by the tempering treatment.

case, the characteristics of the starting microstructures as well as the $T-t$ couple will define which microstructure destabilization mechanisms are activated and ultimately modulate the properties of the microstructure thus obtained [4,6–11].

The motivation for this work is to carry out a rigorous comparative analysis of the tempering behaviour of bainitic and martensitic microstructures in a medium C (0.38 wt%) high Si (3.2 wt%) steel. The study aims to elucidate the different phases and variations in the evolution of these microstructures towards the equilibrium as tempering temperature (200–650 °C) increases. For this purpose, in-situ experimental methods such as high resolution dilatometry together with scanning electron microscopy (SEM), X-ray diffraction (XRD), hardness measurements and theoretical calculations will be used.

2. Materials and experimental methods

2.1. Material and heat treatments

For this investigation a bainitic steel with a medium-carbon high-silicon content, see Table 1, was selected. The steel was developed by the authors in previous studies [12–15]. Among others, the high silicon content (3.2 wt%) and aluminium (0.105 wt%) serve the purpose of retarding or even preventing cementite (θ) precipitation during bainitic transformation and tempering treatments [16–21]. In addition, the alloy also contains 2.56% Mn to ensure low bainite and martensite start temperatures (B_s and M_s) and to enhance the austenite stability [22–25].

To achieve the desired bainitic microstructure, the samples were fully austenitized at a heating rate (HR) of 10 °C/s to 900 °C (T_γ) for 5 min (t_γ). Then were cooled to 325 °C (T_{Iso}) at 10 °C/s, above the experimental M_s, Table 1, and isothermally held for 3 h (t_{Iso}), to ensure completion of the bainitic transformation. Finally, the specimens were cooled down to room temperature with a cooling rate (CR) of 10 °C/s. The martensitic microstructure was obtained by austenitization at analogous $T_\gamma - t_\gamma$ and HR followed by quenching to room temperature at 10 °C/s. The two microstructures were then tempered in the range of 200–650 °C (T_{Temp}), reached at 5 °C/s, in steps of 50 °C, held for 1 h (t_{Temp}), and then cooled down at 10 °C/s to room temperature. Fig. 1 shows a scheme summarising the heat treatments. The design and selection of actual conditions for the treatments are described in detail later in the manuscript.

The heat treatments were carried out using a high-resolution quenching dilatometer, Bahr 805A (TA Instruments, Hull, Germany). The dilatometer also recorded any phase transformations that occurred during the thermal cycles by measuring the relative change in length (RCL) of the specimen. Heat was provided by an induction coil, while helium was used for cooling. The specimen temperature was constantly monitored with a K-type thermocouple spot-welded on the sample surface at mid-length. Cylindrical samples measuring 10 mm in length, and 4 mm in diameter were used for this purpose. Fused silica push-rods, in contact with the samples, with a thermal expansion coefficient of 0.54×10^{-6} °C^{-1}) and a LVDT (linear variable differential transducer) were used to record the length variations [26,27].

Thermal expansion coefficient (TEC) refers to the slope of the plot RCL vs temperature measurement over a given temperature range. In this work, the TEC values are analyzed on heating and cooling, respectively up to and after the isothermal tempering stage, so the following considerations were taken into account when selecting the temperature range. Firstly, to have sufficient data to obtain reliable results. Secondly, to minimize the effect of the temperature dependence of TEC [28,29], an attempt was made to ensure that the temperature range over which the TEC was measured was always the same. Finally, regions where major transformations take place (such as martensite on cooling) should be avoided. Therefore, the temperature ranges for calculating the TEC are as follows: i) 50–150 °C for T_{Temp} = 200 °C, ii) 100–200 °C for T_{Temp} = 250 °C, iii) 100–200 °C for T_{Temp} = 300 °C, iv) 150–300 °C for T_{Temp} = 350 °C, v) 150–250 °C for T_{Temp} = 400 °C, vi) 200–400 °C for T_{Temp} = 450 °C, and vii) 200–450 °C for T_{Temp} = 500–650 °C.

2.2. Microstructural investigations

The identification and evolution of the microstructural constituents after the various treatments were done by means of FEG-SEM observations, ZEISS-SIGMA (Carl Zeiss, Milan, Italy), operating at 10 kV. Specimens were prepared following the standard metallographic procedures, that included grinding with SiC papers (from 320 to 2000 grit) and subsequent polishing with 3 and 1 μm polycrystalline diamond pastes. Finally, the microstructure was revealed using a 2% Nital etching solution. Multiple etching and polishing cycles were carried out to remove the deformed layer induced by grinding, thus improving the definition of the microstructural characteristics and eliminating the martensite that could have formed due to the TRIP (Transformation-Induced Plasticity) effect of the austenite.

The volume fractions of retained austenite (V_γ) and ferrite (V_α) at room temperature (RT) were determined from X-ray diffraction (XRD) patterns recorded with a Bruker D8 Advance diffractometer equipped with Co radiation, a Goebel mirror and a LynxEye position sensitive detector. XRD data were collected using 40 kV and 30 mA as tube setting in the coupled θ-2θ operational mode over a range from 35 to 135° with a step size of 0.015°, and a counting time of 2s per step. Full XRD patterns were analyzed by the Rietveld [30] refinement method using the version 4.2 of the TOPAS software from Bruker AXS and a crystallographic model that includes the standard structure reported elsewhere for ferrite and austenite. The refined parameters included the lattice parameters, scale factors, background and a two theta offset. In the case of steels, phase quantification using Rietveld analysis can be challenging due to the presence of crystallographic texture that can drastically change the measured intensities of the diffraction peaks from their theoretical values. The error associated to the texture effect can been corrected accurately by using the generalized spherical harmonic expansion model without extra information obtained from pole figures. Finally, crystallite size and lattice strain were determined simultaneously from the line broadening of the XRD reflections by the double Voigt approach [31]. For this analysis, the instrumental line broadening

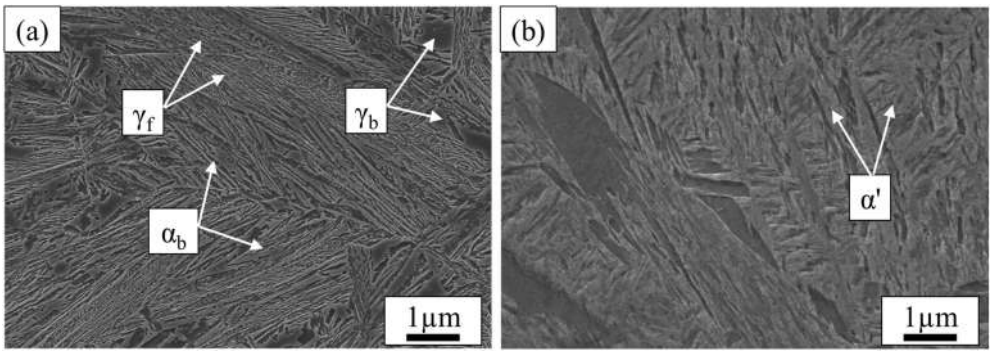

Fig. 2. Scanning electron micrographs of the initial microstructures (a) bainitic microstructure obtained after isothermal transformation at 325 °C for 3 h, (b) martensitic microstructure after cooling to room temperature from 900 °C.

Table 2
Volume fractions (±3%) and carbon content of: retained austenite ($V\gamma$, C_γ ±0.05%) and bainitic/martensitic ferrite ($V_{ab/\alpha'}$ $C_{ab/\alpha'}$ ±0.03%), and bainitic/martensitic ferrite dislocation densities (ρ) obtained from XRD analysis. Hardness (HV_{10}) values for the initial microstructures.

Microstructure	$V\gamma$ (%)	$V_{ab/\alpha'}$ (%)	C_γ (wt.%)	$C_{ab/\alpha'}$ (wt.%)	ρ (m^{-2})	HV_{10}
Bainite	23	77	1.21	0.16	1.98×10^{15}	450 ± 5
Martensite	6	94	0.68	0.29	5.17×10^{15}	640 ± 5

effects were eliminated from the diffraction lines using a empirically parametrized instrument function determined from the diffraction pattern of a well-crystallized corundum plate. It should be remarked that the values obtained for crystallite size and microstrain present a limited reliability (ranging from 10 to 20%) associated with a large standard deviation for the crystallite size in the sample, the assumption of a particular average shape for the crystallite or the presence of defects like stacking and twin faults that give rise to anisotropic size broadening. The lattice parameter of the austenite and ferritic phases were considered to calculate their corresponding carbon contents according to $a = 0.3573 + 0.00075\ C_\gamma(\text{at.\%})$ [32] and $c/a = 1 + 0.045\ C_\alpha(\text{wt.\%})$ [33,34] respectively. Furthermore, the dislocation density (ρ) was also deduced from the values of crystallite size (D) and microstrains (ε) as $\rho = \frac{3\sqrt{2\pi}}{D\,b}\langle\epsilon^2\rangle^{1/2}$ [35].

Vickers hardness measurements (HV_{10}) were performed following the ASTM E92-17 standard [36]. The reported values are the average of at least five measurements.

3. Initial microstructures and design of tempering treatments

3.1. Initial microstructures

The initial bainitic and martensitic microstructures prior to tempering are shown in Fig. 2a and b respectively. The bainitic microstructure, isothermal treatment at 325 °C, consists of the typical mixture of bainitic ferrite plates (α_b), with thicknesses ranging between 44 and 122 nm, and carbon-enriched retained austenite (γ) with its twofold morphology: i) films located between the bainitic ferrite plates (γ_f), and ii) blocks (γ_b), trapped between the sheaves of bainitic [21,37], see Fig. 2a. On the other hand, after quenching to room temperature, a complete lath martensitic microstructure was obtained. It is necessary to mention that in both cases, bainitic and martensitic microstructures, no other phases than those pursued were detected, reflecting that the chosen CR (10 °C/s) was sufficient to avoid any intermediate transformation [12–14].

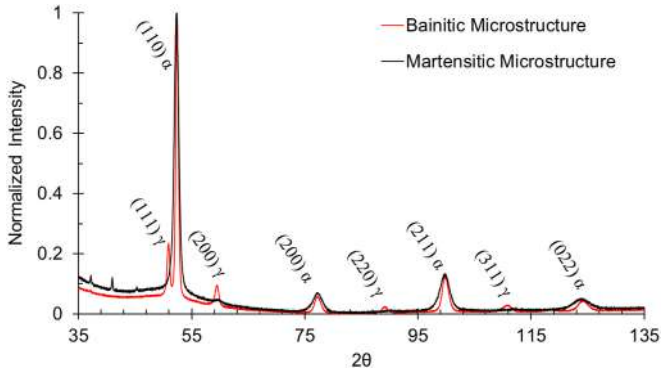

Fig. 3. XRD patterns of the initial bainitic and martensitic microstructures.

The results of the XRD analysis for both microstructures are summarised in Table 2 and the corresponding diffraction patterns in Fig. 3. The analysis shows that, the bainitic ferrite matrix (77%) with a dislocation density of 1.98×10^{15} m^{-2} has a carbon content of 0.16 wt%, which is consistent with its crystal structure being body centred tetragonal (bct) [38–40]. The retained austenite is carbon enriched with a calculated value of 1.21%.

Although this microstructure is considered essentially carbide-free at these levels of Si, advanced characterisation techniques such as APT and synchrotron radiation have detected a few transition iron carbides and cementite (θ) particles within the bainitic ferrite plates in similar steels and treatments [41]. Therefore, their presence, albeit in very small quantities, cannot be ruled out.

In the martensitic microstructure, some retained austenite (6%) was detected with a carbon content of 0.68 wt%. The martensitic ferrite ($\acute{\alpha}$) shows clear signs of having undergone autotempering upon cooling [42–44], with a lower C content, 0.29 wt%, than that of bulk [45–47], but still higher than that of the bainitic ferrite.

As expected the measured dislocation density in the martensitic microstructure (Table 2) is higher than that obtained in the bainitic case, see e.g. Ref. [48].

The hardness values for the two microstructures are 450 HV_{10} and 640 HV_{10} respectively, Table 2.

3.2. Design of tempering treatments

Dilatometric tests were conducted to measure the relative change in length (RCL) and its derivative (DRCL) while heating the bainitic and martensitic microstructures from room temperature to the fully austenitic field, 900 °C, see Fig. 4. The RCL vs. temperature dilatometric data in Fig. 4a, show a linear thermal expansion up to around 500 °C. The different slopes correspond to distinct thermal expansion coefficients (TEC) of the bainitic ($\alpha_b + \gamma$) and martensitic ($\acute{\alpha} + \gamma$)

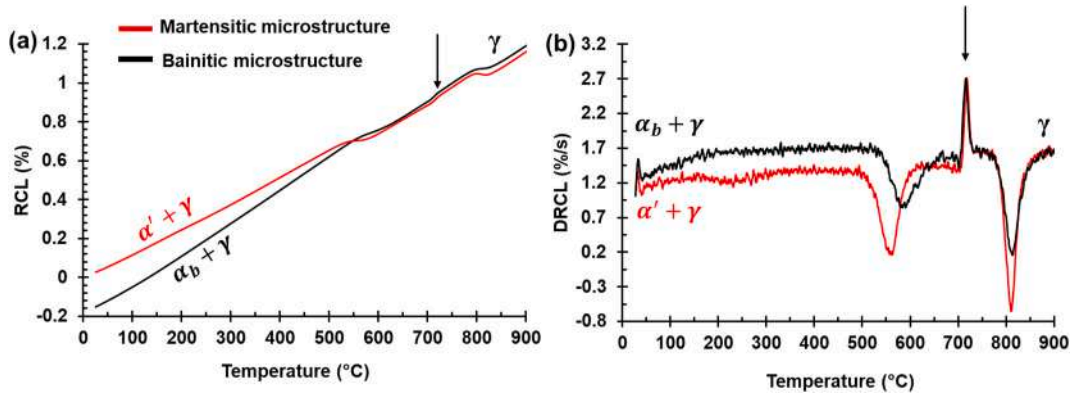

Fig. 4. Dilatometric results during continuous heating up to austenitization temperature for all steels: (a) relative change in length (RCL) and (b) first derivate (DRCL). The vertical arrow indicates the Curie temperature T_C.

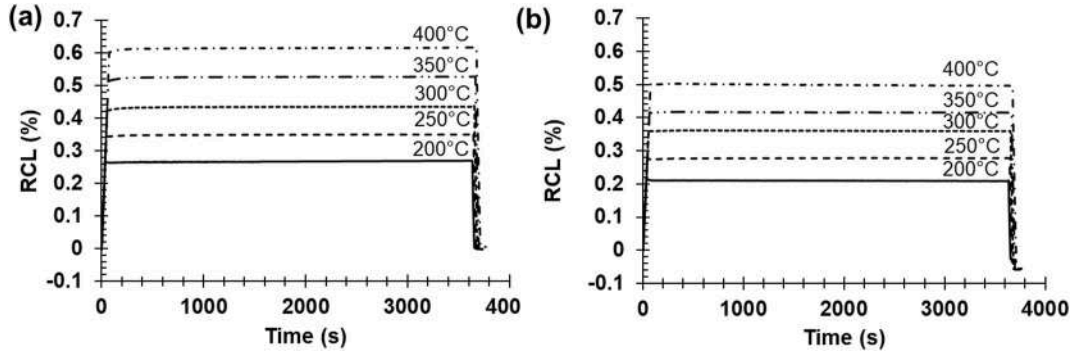

Fig. 5. Relative change in length (RCL) as a function of time for the (a) bainitic and (b) martensitic microstructure in the T_{Temp} range 200–400 °C.

microstructures [49,50]. Both curves exhibit a common anomaly in the form of spontaneous expansion at approximately 730 °C, arrow in Fig. 4, which corresponds to the Curie temperature T_C [51].

In the austenitic field, ~800–900 °C, the RCL curves run parallel, indicating that the thermal expansion coefficient is the same for both cases.

Above 500 °C both microstructures show a contraction in the RCL curves, which is expected to be due to the decomposition of the microstructures. The contraction differs in T range and intensity, between the two cases.

The DRCL curves in Fig. 4b, more sensitive to microstructural changes than the RCL curve, confirm the main changes described earlier and also reveal some subtle ones. Around 200 °C, the martensitic microstructure experiences a decrease in the length change rate due to a contraction, which is not evident in the RCL curves. However, the bainitic microstructure remains unchanged.

Therefore, in an attempt to separate the reactions occurring during the decomposition of bainite and martensite during tempering, isothermal experiments were carried out for 1 h at intervals of 50 °C within the range of T_{Temp} = 200–650 °C.

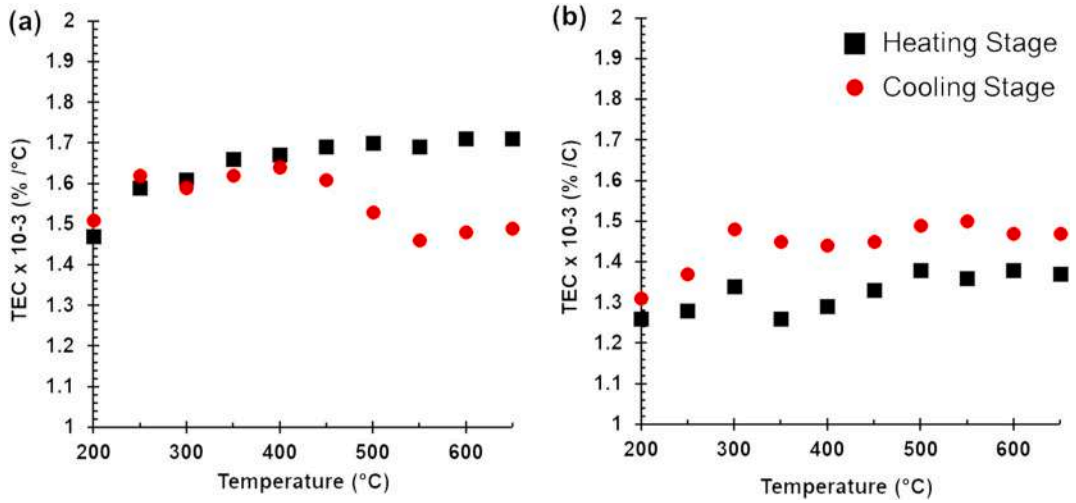

Fig. 6. Evolution of the measured thermal expansion coefficient (TEC) during heating and cooling, to and from each T_{Temp} for the (a) bainitic and (b) martensitic microstructure.

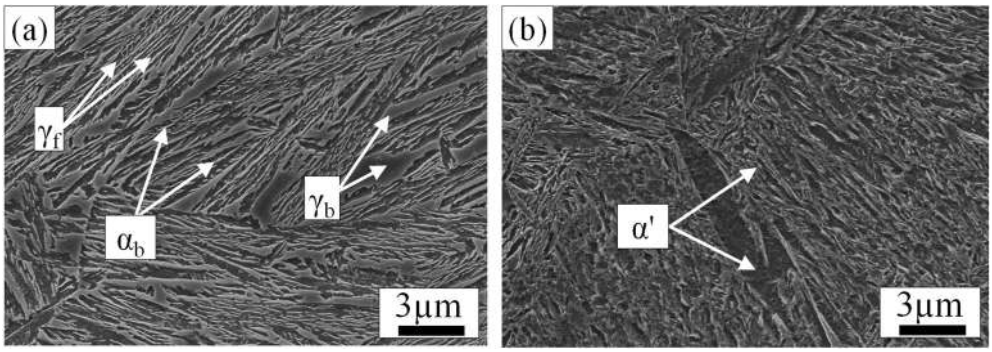

Fig. 7. Scanning electron micrographs of the microstructures obtained after tempering at 350 °C the initial (a) bainitic microstructure and (b) martensitic microstructure. α_b: bainitic ferrite, γ_f: filmy retained austenite, γ_b: blocky retained austenite, $\acute{\alpha}$: martensite.

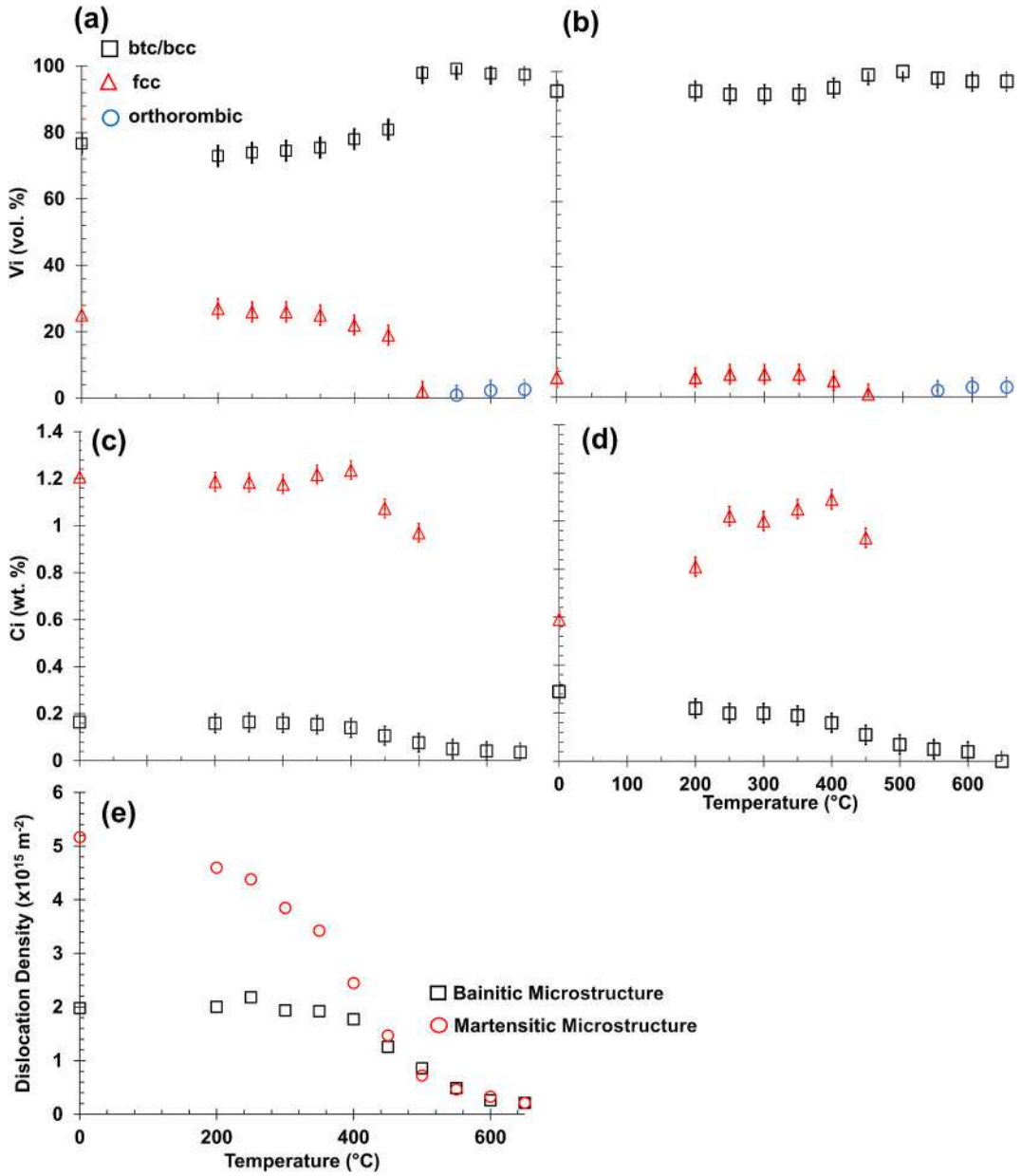

Fig. 8. XRD results as a function of the tempering temperature for both initial microstructures, i.e. bainite (a) & (c) and martensite (b) & (d). Volume fraction (V_i%) and carbon contents (C_i wt.%) of the phases identified, bcc/bct refers to ferritic phases, fcc to austenite and orthorhombic to cementite. (e) dislocation density of the ferritic phase for the bainitic and the martensitic microstructure.

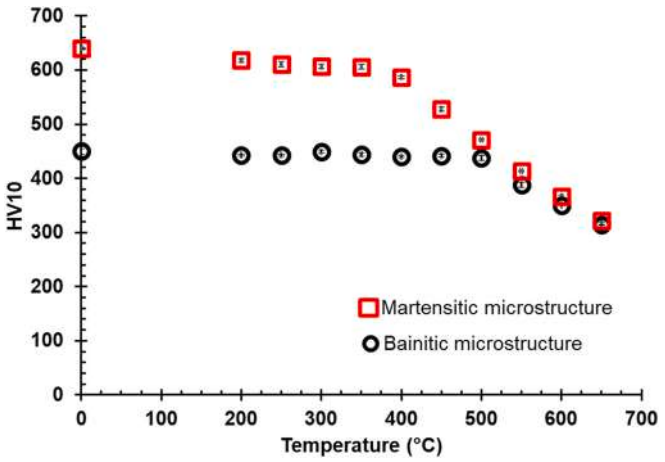

Fig. 9. Temperature evolution of hardness Vickers (HV10) during tempering of the bainitic and martensite initial microstructures.

4. Results and discussion

4.1. Microstructural evolution during tempering between 200 and 400 °C

Fig. 5a and b illustrate the changes in RCL over time during the tempering cycle for the bainitic and martensitic microstructures, respectively, in the T_{Temp} range of 200–400 °C. It is observed that bainite maintains linearity during heating and cooling, Fig. 5a, which can be attributed to its thermal expansion coefficient (TEC). The TECs calculated during heating and cooling, to and from each T_{Temp}, are shown in Fig. 6. The results show that the values are almost identical, suggesting that the microstructures should be the same before and after the isothermal step. During the 1 h isothermal stage, the RCL curves remain almost flat and unchanged, supporting the previous suggestion and in agreement with previous studies on bainitic microstructures [8]. The measured ΔRCL values during the isothermal step are ≤0.013%, and can be attributed to drifting during the measurement, usually associated with thermal interaction at the contact point between the push-rod and the sample, especially during isothermal dwells.

SEM and XRD results confirm the stability of the bainitic microstructure in this T_{Temp} range, 200–400 °C. The microstructure remains

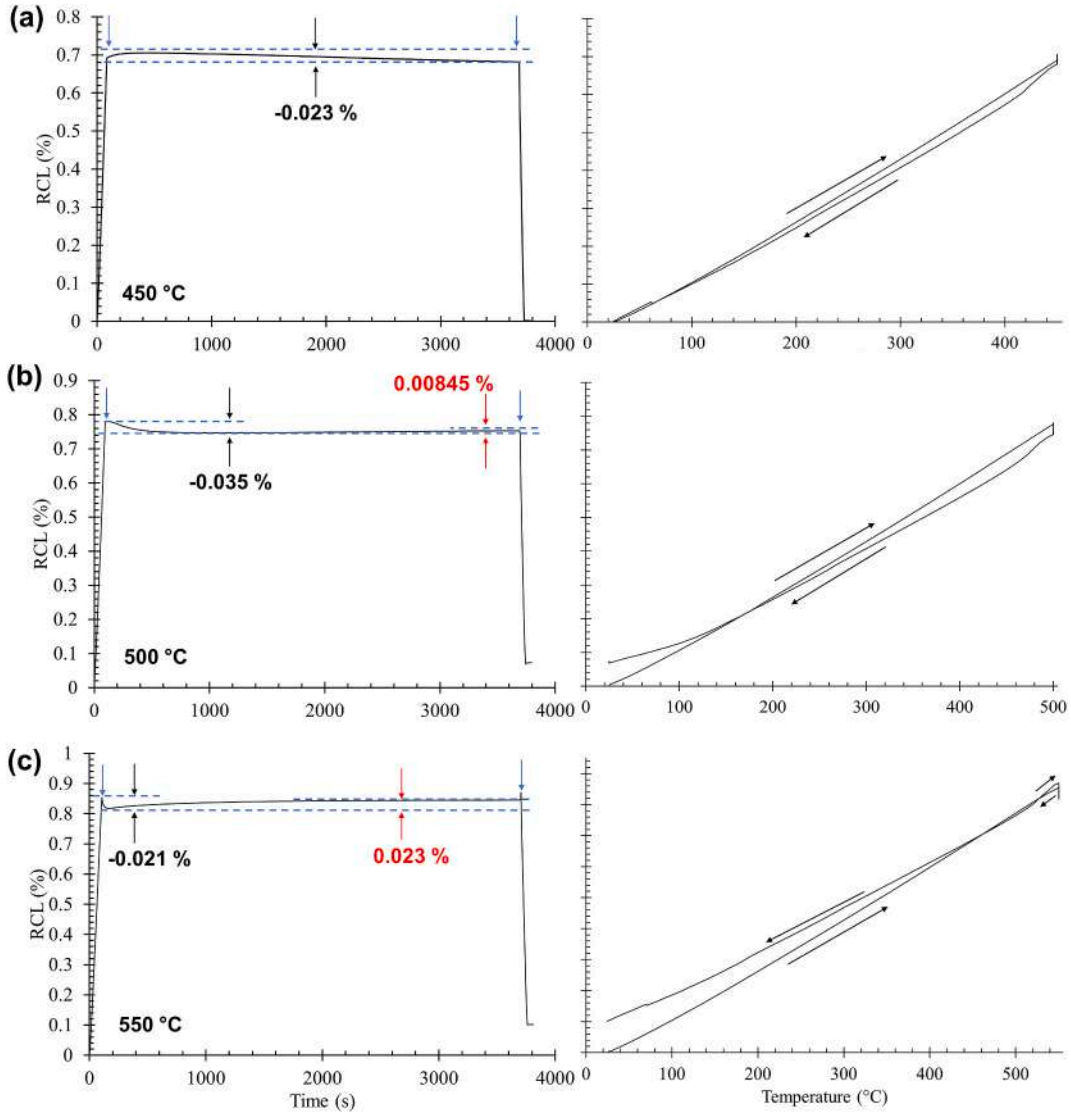

Fig. 10. Relative change in length (RCL) as a function of time and temperature for the bainitic microstructure tempered at (a) 450 °C, (b) 500 °C, and (c) 550 °C. In the figure the blue arrows indicate the beginning and the end of the isothermal stage, while the dashed lines with black and/or the red arrows indicate the first and the second, if present, contraction/expansion occurring during the isothermal stage.

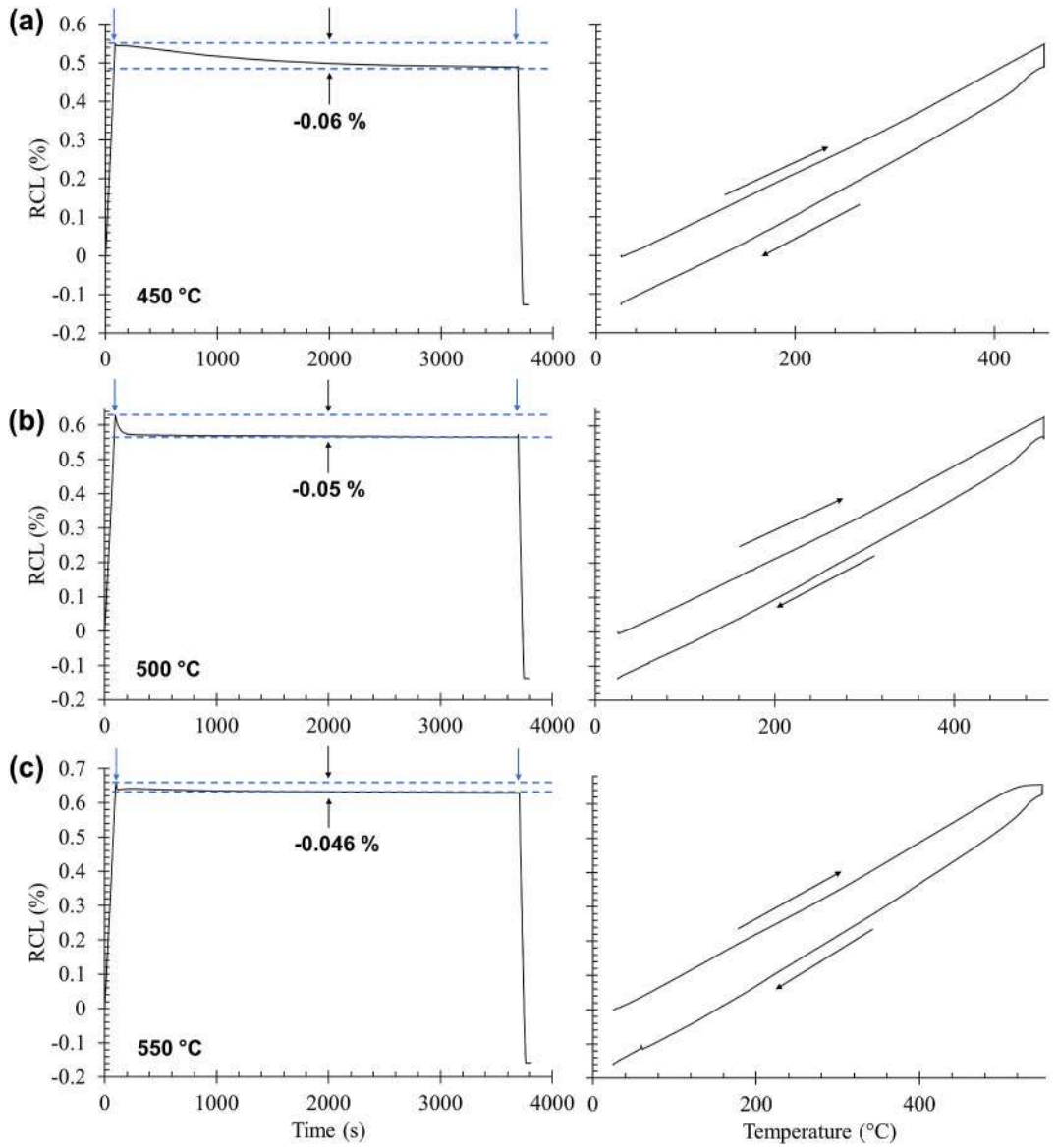

Fig. 11. Relative change in length (RCL) as a function of time and temperature for the martensitic microstructure tempered at (a) 450 °C, (b) 500 °C, and (c) 550 °C. In the figure the blue arrows indicate the beginning and the end of the isothermal stage, while the dashed lines with black and/or the red arrows indicate the first and the second, if present, contraction/expansion occurring during the isothermal stage.

virtually identical to the starting microstructure, as shown in Fig. 7 in comparison to Fig. 2. The phase distribution, carbon content, and dislocation density also remain relatively constant throughout the range, as seen in Fig. 8, as do the HV_{10} values in Fig. 9.

For the case of the martensitic microstructure, during both the heating and cooling ramp, linearity is also maintained, Fig. 5b, but subtle changes occur on heating in the 200 °C–400 °C T_{Temp} range. The variations detected are consistent with the widely reported onset of martensite tempering by the precipitation of transition carbides and some carbon partition from supersaturated martensite to austenite [6,7,52], both leading to contractions in dilatometry [26]. What is more, if in a microstructure such as bainite, which does not undergo changes during tempering at these temperatures, a small expansion is detected in the isothermal step, in the case of martensite, it is a contraction ($\Delta RCL \leq -0.006\%$.). Therefore, this contraction can only be the net result of the aforementioned expansion and the contraction resulting from the precipitation and carbon redistribution processes which, activated during heating, continues in the isothermal stage. By observing the measured TECs on heating and cooling, Fig. 6, we found that they are indeed different and therefore correspond to microstructures that are different at the beginning of the tempering and at the end of the isothermal step.

Transition carbides were not detected by SEM, Fig. 7b, or XRD, Fig. 8 due to their small size and low volume fraction. However, XRD analysis revealed that while there was no change in the martensite or austenite fraction within the margins of error, the carbon content of martensite decreased slightly while that of austenite increased. This supports the process of precipitation and carbon redistribution activated in this temperature range. The whole process is accompanied by a decrease of the dislocation density [53,54], Fig. 8, and the expected mild softening of the microstructure, as revealed by the HV_{10} values in Fig. 9.

4.2. Microstructural evolution during tempering between 450 and 550 °C

Although on heating the bainitic microstructure to temperatures between 450 and 500 °C does not appear to cause any microstructural changes as the linearity of the RCL curves is maintained, Fig. 10, once T_{Temp} is reached it can be observed that a contraction is recorded. At 450 °C this contraction ($\Delta RCL = -0.023$ %) lasts throughout the

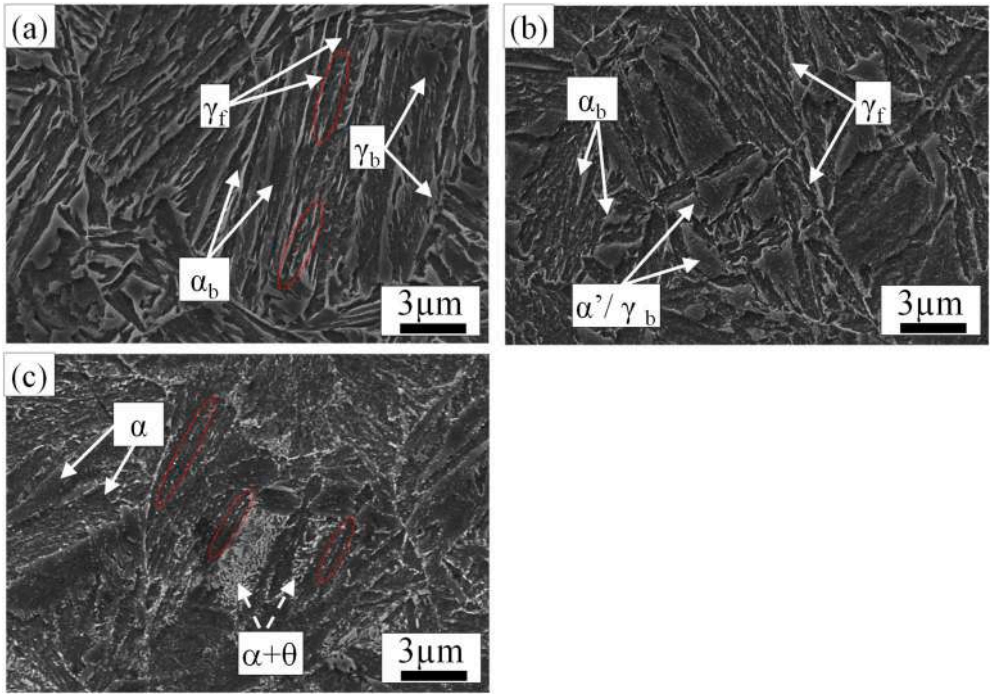

Fig. 12. Scanning electron micrographs of the microstructures obtained after tempering the initial bainitic microstructure (a) at 450 °C, (b) at 500 °C, (c) at 550 °C. α_b: bainitic ferrite, γ_f: filmy retained austenite, γ_b: blocky retained austenite, $\acute{\alpha}$: martensite, α: ferrite, θ: cementite. The white dotted arrows indicate the mixture of cementite and ferrite formed from the decomposition of the austenite blocks; while the red dotted frames denote the cementite particles at the bainitic ferrite phase boundaries.

treatment, whereas at 500 °C (ΔRCL = −0.035 %) it occurs in the first 15 min, after which the signal stabilises, and a subtle increase happens over time until the end of the treatment (ΔRCL = 0.00845 %). For the 550 °C treatment, such contraction starts during heating, and rapidly finalises, 1 min, once at T_{Temp} (ΔRCL = −0.021%), being followed by a brief period of signal stability. This is then succeeded by an expansion (ΔRCL = 0.023%) before the signal stabilises once more.

The changes in the dilatometric signal, as described, would be consistent with the following processes. The initial contraction at T_{Temp}, would be attributed to the partial decomposition of retained austenite films, between the bainitic ferrite plates, into ferrite and cementite, see the red dotted framed examples in Fig. 12a showing carbide arrays at the bainitic ferrite plate boundaries. Such austenite is characterized for having a greater driving force for carbide precipitation [8,55–57] as compared to the blocks, due to their also higher C content [58–60]. Fig. 8 shows that at 450 °C there is a decrease on the fraction of austenite and a decrease in the C content of both, ferrite and austenite.

Those austenite films begin to decompose during heating to 500 and 550 °C holding temperatures, so, once isothermal holding begins, the decomposition process, already triggered, is quickly over.

Prior to the decomposition of the blocky austenite into a mixture of ferrite and cementite, it undergoes an intermediate stage in which it loses C in the form of precipitation [5,26], resulting in expansions at 500 and 550 °C, and compatible with the martensitic transformation detected at approximately 100 °C and 150 °C respectively, Fig. 10, indicating that the austenite has been depleted in C to levels that make it unstable at room temperature. The results in Fig. 8 should be interpreted as having been carried out at room temperature, with partial or total transformation of the remaining austenite (at the end of the isothermal step at T_{Temp}) to martensite. Even though, as shown in Fig. 10, the measured Ms temperature increases as the tempering temperature is increased, indicating that martensite is produced from an austenite with a lower C content, Fig. 8.

The next natural step for this C-depleted austenite blocks is to finally decompose into a mixture of ferrite and cementite at higher T_{Temp}, as indicated by dotted arrows in Fig. 12c, leading to an expansion in the RCL curves.

Complete decarburisation of supersaturated ferrite requires the precipitation of carbide from C trapped in dislocations [61–63]. However, this requires the removal of some dislocations by recovering during tempering. Carbon is more stable when segregated to dislocations than in transition carbides or cementite [63]. Therefore, the high dislocation density is then stabilised by carbon pinning, which strongly inhibits the recovery of the dislocation network. As a result, carbide precipitation from bainite occurs gradually and is very sluggish as the tempering temperature increases. During this process, bainitic ferrite loses its tetragonal character and the final structure consists of cementite and a defect-free bcc ferrite matrix. This process causes a small contraction, which is an order of magnitude smaller than the contractions/expansions related to austenite decomposition, and may be overshadowed by them [26]. From the results in Fig. 8 it is clear that the destabilization of the bainitic ferrite has taken place at 550 °C, where the decrease of the dislocation density in the ferrite is accompanied by a decrease of the carbon in ferrite and the detection, for the first time, of the presence of cementite in the XRD analysis. This cementite also comes from austenite destabilization processes, but the major contribution is expected to come from the bainitic matrix which represents almost 80% of the microstructure.

Obviously, the difference in TEC values on heating and cooling becomes greater as T_{Temp} increases and more decomposition events are completed/initiated, increasing the differences between the two microstructures.

In bainitic microstructures the thickness of the bainite plates dominates the overall strength, and the decomposition of thin films of retained austenite results in cementite precipitation at the bainite plate boundaries, thereby pinning them [55,64,65], see some examples in Fig. 12c denoted by red dotted frame. Therefore, there is a big resistant to the loss of hardness until tempering leads to a loss of the plate shape. Fig. 9 shows that the hardness values remain almost constant up to 500 °C with a small decrease at 550 °C. The additional contributions of

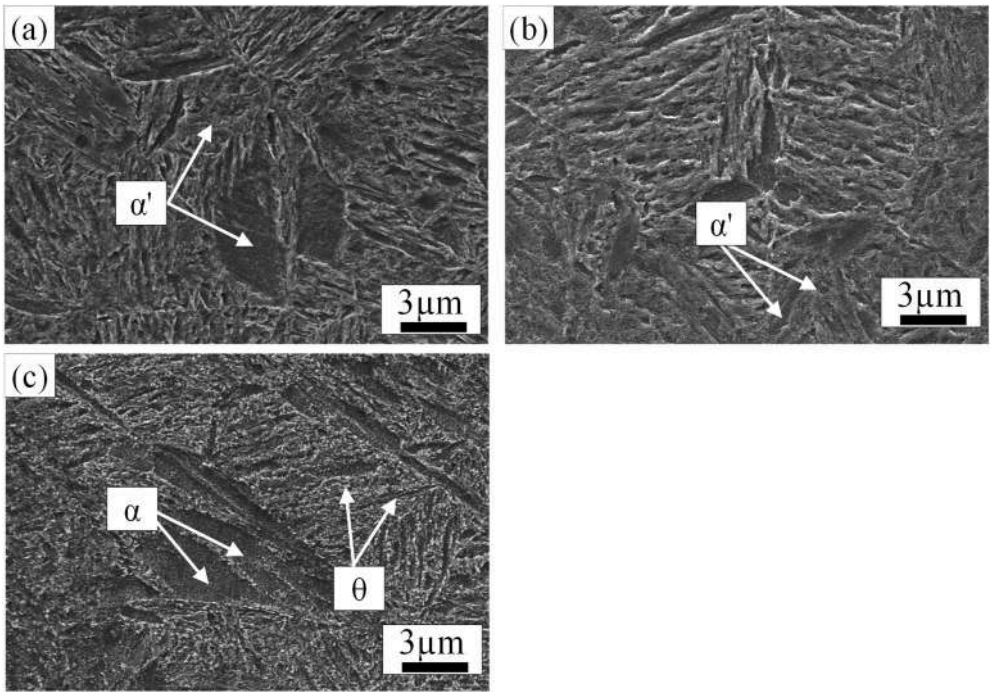

Fig. 13. Scanning electron micrographs of the microstructures obtained after tempering the initial martensitic microstructure (a) at 450 °C, (b) at 500 °C, (c) at 550 °C. *á*: martensite, θ: cementite.

dislocation density, precipitation and martensite should be also considered when analysing the evolution of hardness.

For the martensitic microstructure tempered at T_{Temp} = 450 °C, the material contracts continuously by ΔRCL = −0.06%. At 500 °C this contraction (ΔRCL = −0.05%), is completed in 180s, see Fig. 11 regarding the T_{Temp} = 550 °C case, the contraction that was already evident during the last stages of heating to T_{Temp} is quickly completed once at the targeted temperature.

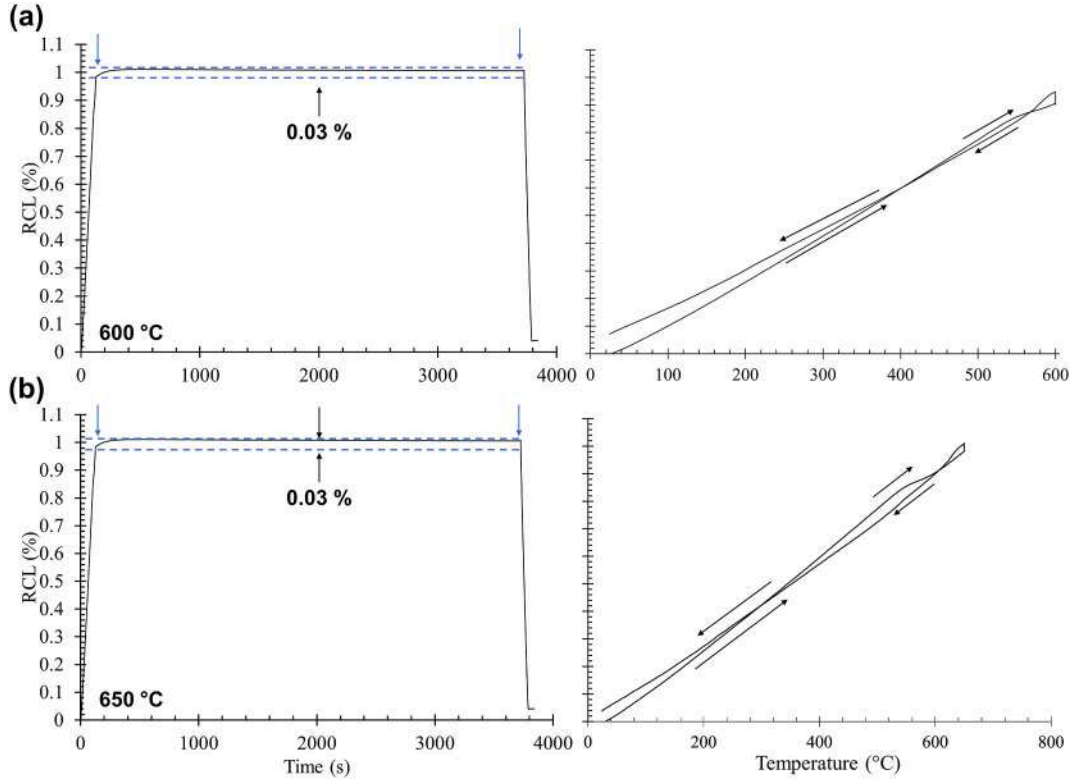

Fig. 14. Relative change in length (RCL) as a function of time and temperature for the bainitic microstructure tempered at (a) 600 °C and (b) 650 °C. In the figure the blue arrows indicate the beginning and the end of the isothermal stage, while the dashed lines with black and/or the red arrows indicate the first and the second, if present, contraction/expansion occurring during the isothermal stage.

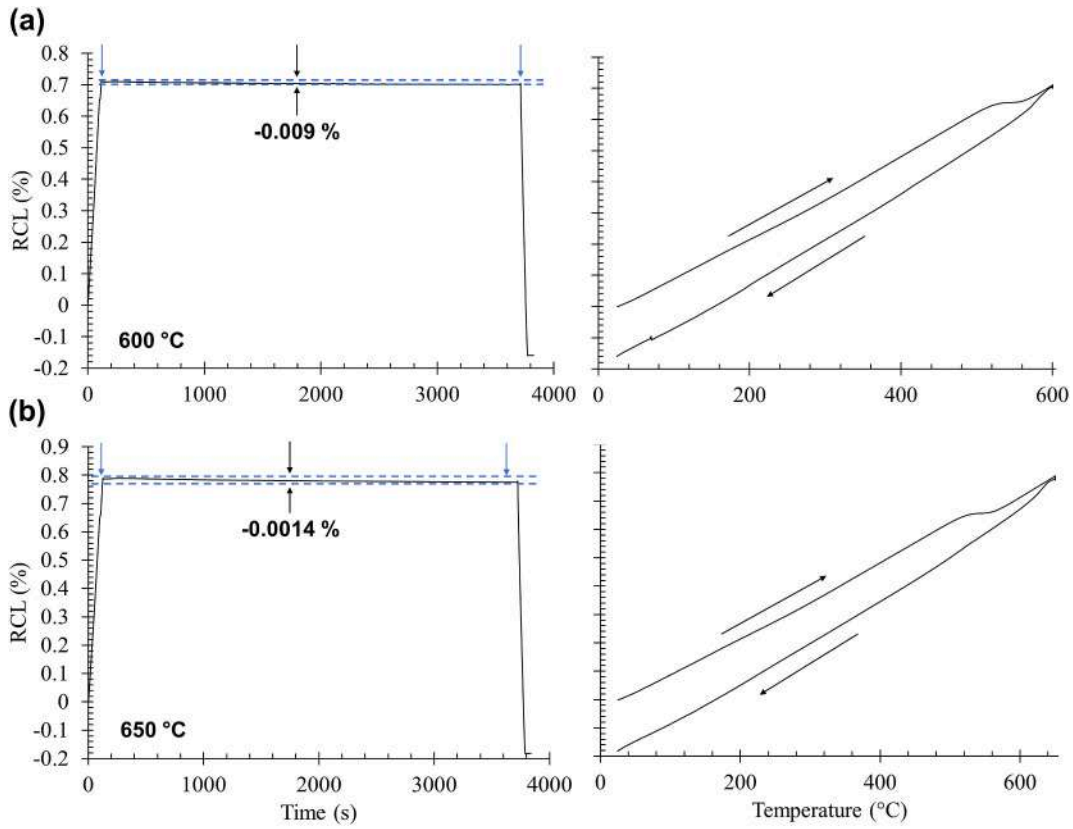

Fig. 15. Relative change in length (RCL) as a function of time and temperature for the martensitic microstructure tempered at (a) 600 °C and (b) 650 °C. In the figure the blue arrows indicate the beginning and the end of the isothermal stage, while the dashed lines with black and/or the red arrows indicate the first and the second, if present, contraction/expansion occurring during the isothermal stage.

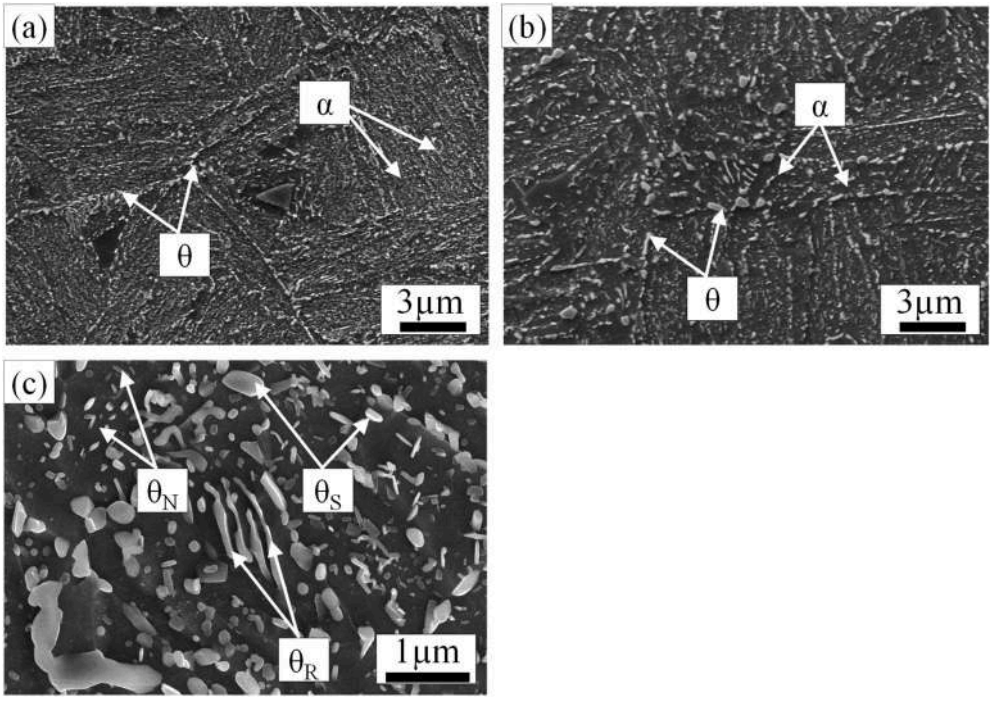

Fig. 16. Scanning electron micrographs of the microstructures obtained after tempering the initial bainitic microstructure (a) at 600 °C, (b) and (c) at 650 °C. *α*: ferrite, θ: cementite, θ_N: needle-like cementite, θ_R: rod-like cementite, θ_S: spherical cementite.

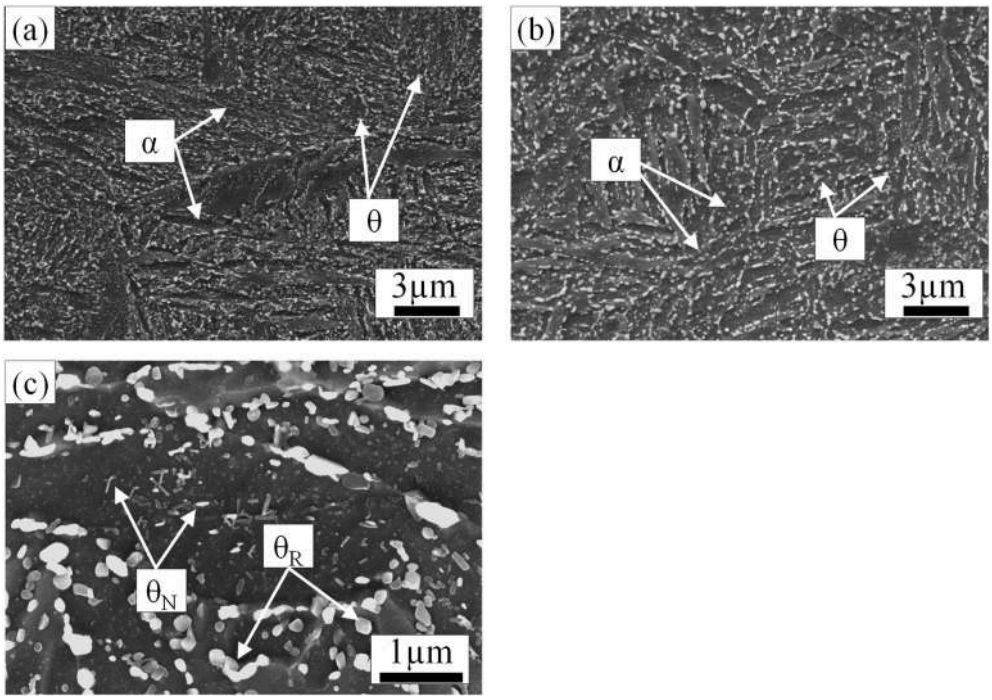

Fig. 17. Scanning electron micrographs of the microstructures obtained after tempering the initial martensitic microstructure (a) at 600 °C, (b) and (c) at 650 °C. *α*: ferrite, θ: cementite, θ_N: needle-like cementite, θ_R: rod-like cementite.

Similar to the bainitic microstructure, the contractions in this case are caused by the partial decomposition of retained austenite films between the laths of martensite, but mainly due to the further destabilization of the ferritic martensite. Fig. 8 shows a decrease in the fraction of austenite and a decrease in the C content of both, ferrite and austenite at 450 °C. The results indicate that tempering the martensite at 500 °C and 550 °C leaves no austenite at room temperature. Instead, a ferritic matrix with decreasing C content in solid solution is observed, with cementite precipitates only detectable at 550 °C. Throughout the T range, the dislocation density in the ferrite decreases. By tempering at 450 °C, the destabilization process causes the microstructure to become blurred and the grain boundaries to become fuzzy [66], Fig. 13a. As the temperature increases to 500 °C, Fig. 13b, few small precipitated carbides appear within the matrix. Tempering at 550 °C results in a mixture of ferrite and spherical cementite particles, as shown in the SEM micrograph in Fig. 13c.

The mentioned intermediate state, in which part of the austenite loses carbon through precipitation before complete decomposition, also occurs in the martensitic microstructure. This is evidenced by its transformation into fresh martensite upon cooling, as shown for the 550 °C case in Fig. 11.

The mentioned microstructural changes are reflected in the different TEC values on heating and cooling, as well as in the expected softening of the microstructure, Figs. 6 and 9 respectively.

4.3. Microstructural evolution during tempering between 600 and 650 °C

During heating of the bainitic microstructure to the two highest chosen T_{Temp}, 600 °C and 650 °C, the previously mentioned destabilization processes are almost completed. While at 600 °C, after a very sharp contraction, Fig. 14 a, due to bainitic ferrite destabilization, an expansion (ΔRCL = 0.03%) that is completed in approximately 1000s, from the decomposition of blocks of austenite, gives way to a plateau. In the case of the 650 °C, such expansion is also ΔRCL = 0.03% and stabilises in approximately 400s.

Regarding the martensitic microstructure, it is observed that the microstructure is fully destabilised during heating at the two specified temperatures. The isothermal maintenance stage does not show any

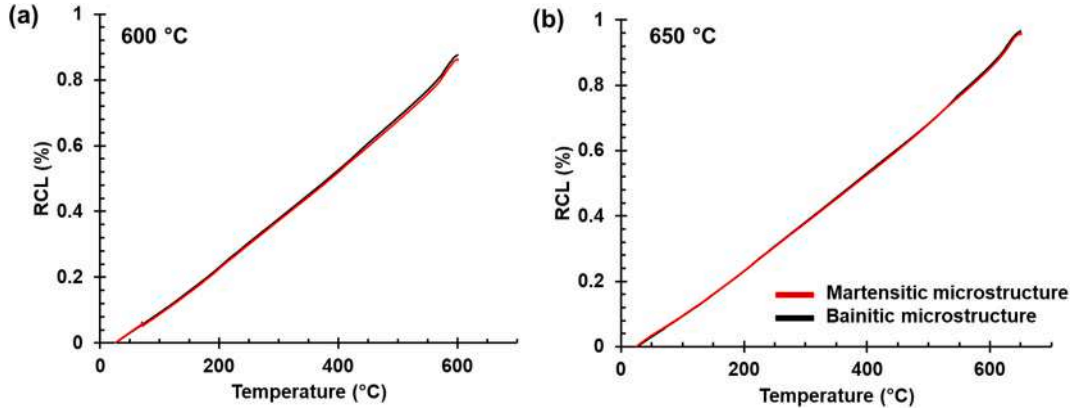

Fig. 18. Relative change in length (RCL) variation upon cooling after tempering the initial bainitic and martensitic microstructure at (a) 600 °C and (b) 650 °C.

changes as the RCL remains constant throughout the treatment, Fig. 15.

It is important to note that the tempering result for the two microstructures at these temperatures is identical. The XRD results in Fig. 8 show that the final microstructure is a mixture of 97% ferrite and 3% cementite. The ferrite has a carbon content corresponding to equilibrium (0.04 wt%) and the dislocation density of a fully restored microstructure [67]. In other words, both microstructures appear to have reached equilibrium.

In both cases, Figs. 16 and 17, cementite precipitates are found in parallel arrays along the prior laths/plates and within them. The morphologies of these precipitates can be needle-shaped (θ_N) or rod-like (θ_R), but the vast majority are spherical (θ_S), with size increasing as T_{Temp} increases [2,68]. Additional data supporting the claim that both microstructures are identical after tempering can be found in the hardness values presented in Fig. 9. These values are the same within the margins of measurement error, as are the TEC values on cooling in Fig. 6. Fig. 18 also demonstrates that the RCL vs. time curves for both microstructures are identical.

Upon closer inspection of the RCL curves, a subtle deviation from linearity around 200 °C can be observed. This is most likely due to the martensitic transformation of austenite blocks that have not previously decomposed. Using the C-balance, it is possible to calculate the expected amount of ferrite and cementite in both microstructures if the entire initial microstructure had decomposed. In both cases, approximately 6% cementite was estimated, which is only half of what was measured. This results in a deficit of about 0.2 wt% with respect to bulk carbon. It is reasonable to assume that there is still a certain amount of austenite untransformed [69–73], transforming to martensite on subsequent cooling to room temperature.

5. Conclusions

In this study, we explore the tempering evolution of two distinct microstructures, bainite and martensite, characterized by tetragonal ferrite and retained austenite matrices with notable differences in fractionation and characteristics. The journey towards an equilibrium microstructure, comprising ferrite, cementite, and retained austenite at elevated temperatures, unveils some insights into the interplay of initial microstructural disparities.

In bainite, where retained austenite constitutes a significant fraction (~25%) with a high carbon content (1.2 wt%), its pivotal role is evident. Contrastingly, in martensite, with a lower austenite fraction (6%) and lesser carbon content (0.68% wt.%), the influence of austenite is comparatively limited. Here, the ferritic matrix, characterized by a high carbon content and significant dislocation density, emerges as the primary determinant.

The divergence in tempering paths stems from these initial disparities. In bainite, stable up to 400 °C, the thin-films of retained austenite, with high carbon content, undergoes destabilization at 450 °C, while in martensite, the precipitation of transition carbides and carbon partitioning from martensitic ferrite to austenite initiates at 200–400 °C. Subsequent tempering processes involve the destabilization of bainitic ferrite and the decomposition of retained austenite into ferrite and cementite, following a phase of partial desupersaturation in carbon through precipitation.

At 600 °C and 650 °C, the completion of the destabilization process leads to the attainment of a final equilibrium microstructure, identical for both initial microstructures. However, it's worth noting that the retained austenite in both microstructures may not have completely decomposed, as indicated by the microstructural and dilatometric analysis.

The quantitative indicators provided by XRD analysis (dislocation density, carbon content, and retained austenite fraction) between the initial and final microstructures underline the trajectory towards equilibrium. Bainitic microstructures, which are closer to the final equilibrium state, show greater stability and resistance to change compared to martensite, which is further from equilibrium. The convergence towards equilibrium becomes evident at 550 °C, with strong similarities observed between the two microstructures. Ultimately, at 600 °C, equilibrium is achieved, marking the culmination of their tempering journey.

These findings provide valuable insights into the nuanced interplay between microstructural evolution and thermal stimuli in bainitic and martensitic steels, with significant implications for optimizing heat treatment protocols and tailoring material properties to meet diverse industrial requirements.

Funding

This research has been partially funded by Research Fund for Coal and Steel, grant number RFCS-2019-899251.

Declaration of competing interest

The authors declare the following financial interests/personal relationships which may be considered as potential competing interests: Carlos Garcia-Mateo reports financial support was provided by CENIM-CSIC. Carlos Garcia-Mateo reports financial support was provided by Research Fund for Coal and Steel. If there are other authors, they declare that they have no known competing financial interests or personal relationships that could have appeared to influence the work reported in this paper.

Acknowledgements

The authors gratefully acknowledge the support provided by laboratories belonging to CENIM: X-Ray Diffraction, Metallography and Phase Transformations. CG-M would like to express his gratitude to Daniel R. Borrego for his support in all laboratory work.

References

[1] Bhadeshia HKDH, Honeycombe RWK. Steels: microstructure and properties. In: Bhadeshia HKDH, Honeycombe RWK, editors. Steels microstruct. Prop. fourth ed. Butterworth-Heinemann; 2017. p. 488. Fourth Edition.
[2] Bhadeshia HKDH. Bainite in steels. Third. London: CRC Press; 2019. https://doi.org/10.1201/9781315096674.
[3] Krauss G. Heat treated martensitic steels: microstructural systems for advanced manufacture. ISIJ Int 1995;35:349–59. https://doi.org/10.2355/isijinternational.35.349.
[4] Krauss G. Tempering of lath martensite in low and medium carbon steels: assessment and challenges. Steel Res Int 2017;88:1700038. https://doi.org/10.1002/srin.201700038.
[5] Kuntz M, Sourmail T, Garcia-Mateo C, Allain S, Caballero FG, Denand B, et al. Design of new economic secondary precipitating steels for fatigue resistance at elevated service temperatures (SteelSeco). CSIC - Centro Nacional de Investigaciones Metalúrgicas (CENIM) 2021. https://doi.org/10.20350/digitalCSIC/13867.
[6] Cheng L, Mittemeijer EJ. The tempering of iron-Carbon martensite; Dilatometric and calorimetric analysis. Metall Trans A 1990;21:13–26. https://doi.org/10.1007/BF02656420.
[7] Thomson R, Miller M. Carbide precipitation in martensite during the early stages of tempering Cr- andMo-containing low alloy steels. Acta Mater 1998;46:2203–13. https://doi.org/10.1016/S1359-6454(97)00420-5.
[8] Garcia-Mateo C, Caballero FG. Bainitic steels: tempering. Encycl. Iron, steel, their alloy. Taylor & Francis; 2016. p. 1–14. https://doi.org/10.1081/e-eisa-120050640.
[9] Wang X, Zhang X, Fang Q, Ma H, Zhang R, Liu F, et al. Effect of tempering on stability of retained austenite and tensile properties of nanostructured bainitic steel. Mater Sci Eng A 2022;856:143958. https://doi.org/10.1016/j.msea.2022.143958.
[10] Wang X, Liu C, Qin Y, Li Y, Yang Z, Long X, et al. Effect of tempering temperature on microstructure and mechanical properties of nanostructured bainitic steel. Mater Sci Eng A 2022;832:142357. https://doi.org/10.1016/j.msea.2021.142357.
[11] Mandal S, Ghosh P, Rajput AS, Yadav S, Haldar A. Microstructure and property evolution during tempering of a medium carbon bainitic steel. Mater Sci Technol 2024. https://doi.org/10.1177/02670836241240370.
[12] Franceschi M, Bettanini AM, Pezzato L, Dabalà M, Jacques PJ. Effect of multi-step austempering treatment on the microstructure and mechanical properties of a high silicon carbide-free bainitic steel with bimodal bainite distribution. Metals 2021;11. https://doi.org/10.3390/met11122055.

[13] Franceschi M, Pezzato L, Gennari C, Fabrizi A, Polyakova M, Konstantinov D, et al. Effect of intercritical annealing and austempering on the microstructure and mechanical properties of a high silicon manganese steel. Metals 2020;10:1–19. https://doi.org/10.3390/met10111448.

[14] Franceschi M, Pezzato L, Settimi AGAG, Gennari C, Pigato M, Polyakova M, et al. Effect of different austempering heat treatments on corrosion properties of high silicon steel. Materials 2021;14:1–17. https://doi.org/10.3390/ma14020288.

[15] Franceschi M, Yazdanpanah A, Leone D, Pezzato L, Dabalà M. Laser powder bed fusion fabrication of a novel carbide-free bainitic steel: the possibilities and a comparative study with the conventional alloy. Metals 2024;14. https://doi.org/10.3390/met14010113.

[16] Fazeli F, Militzer M. Modelling simultaneous formation of bainitic ferrite and carbide in TRIP steels. ISIJ Int 2012;52:650–8. https://doi.org/10.2355/isijinternational.52.650.

[17] Hulme-Smith CN, Lonardelli I, Peet MJ, Dippel AC, Bhadeshia HKDH. Enhanced thermal stability in nanostructured bainitic steel. Scr Mater 2013;69:191–4. https://doi.org/10.1016/j.scriptamat.2013.03.029.

[18] Qian L, Zhou Q, Zhang F, Meng J, Zhang M, Tian Y. Microstructure and mechanical properties of a low carbon carbide-free bainitic steel co-alloyed with Al and Si. Mater Des 2012;39:264–8. https://doi.org/10.1016/j.matdes.2012.02.053.

[19] Hou X, Xu Y-B, Zhao Y-F, Wu D. Microstructure and mechanical properties of hot rolled low silicon TRIP steel containing phosphorus and vanadium. J Iron Steel Res Int 2011;18:40–5. https://doi.org/10.1016/S1006-706X(11)60115-5.

[20] Bhadeshia HKDH, Load M, Svensson L. Silicon-rich bainitic steel welds. Trans JWRI 2003:43–52.

[21] Garcia-Mateo C, Caballero FG, Sourmail T, Kuntz M, Cornide J, Smanio V, et al. Tensile behaviour of a nanocrystalline bainitic steel containing 3wt% silicon. Mater Sci Eng A 2012;549:185–92. https://doi.org/10.1016/j.msea.2012.04.031.

[22] Bhadeshia HKDH, Honeycombe RWK. Steels and properties. 2017.

[23] Garcia-Mateo C, Sourmail T, Caballero FG, Smanio V, Kuntz M, Ziegler C, et al. Nanostructured steel industrialisation: plausible reality. Mater Sci Technol 2014;30:1071–8. https://doi.org/10.1179/1743284713Y.0000000428.

[24] Garcia-Mateo C, Caballero FG, Sourmail T, Smanio V, De Andres CG. Industrialised nanocrystalline bainitic steels. Design approach. Int J Mater Res 2014;105:725–34. https://doi.org/10.3139/146.111090.

[25] Bhadeshia HKDH. Bainite in steels. Theory and practice. Third. London: Maney Publishing; 2015. https://doi.org/10.1201/9781315096674.

[26] Ruiz-Jimenez V, Kuntz M, Sourmail T, Caballero FG, Jimenez JA, Garcia-Mateo C. Retained austenite destabilization during tempering of low-temperature bainite. Appl Sci 2020;10:8901. https://doi.org/10.3390/app10248901.

[27] Santajuana MA, Rementeria R, Kuntz M, Jimenez JA, Caballero FG, Garcia-Mateo C. Low-temperature bainite: a thermal stability study. Metall Mater Trans A Phys Metall Mater Sci 2018;49:2026–36. https://doi.org/10.1007/s11661-018-4595-2.

[28] Digilov RM. Temperature dependence of thermal expansion of solids: a new approach in the terms of the Lambert function. Phys B Condens Matter 2021;616:413117. https://doi.org/10.1016/j.physb.2021.413117.

[29] Kozlovskii YM, Stankus SV. The linear thermal expansion coefficient of iron in the temperature range of 130-1180 K. J Phys Conf Ser 2019;1382. https://doi.org/10.1088/1742-6596/1382/1/012181.

[30] Young RA. The Rietveld method. Oxford University Press; 1995.

[31] Balzar D, Audebrand N, Daymond MR, Fitch A, Hewat A, Langford JI, et al. Size–strain line-broadening analysis of the ceria round-robin sample. J Appl Crystallogr 2004;37:911–24. https://doi.org/10.1107/S0021889804022551.

[32] Cheng L, Böttger A, de Keijser TH, Mittemeijer EJ. Lattice parameters of iron-carbon and iron-nitrogen martensites and austenites. Scr Metall Mater 1990;24:509–14. https://doi.org/10.1016/0956-716X(90)90192-J.

[33] Honda K, Nishiyama Z. On the nature of the tetragonal and cubic martensites. Sci Reports Tohoku Imp Univ 1932;21:299–331.

[34] Cohen M. The strengthening of steel. Metall Soc TMS AIME 1962;224:638–57.

[35] Dini G, Ueji R, Najafizadeh A, Monir-Vaghefi SM. Flow stress analysis of TWIP steel via the XRD measurement of dislocation density. Mater Sci Eng A 2010;527:2759–63. https://doi.org/10.1016/j.msea.2010.01.033.

[36] Hardness K, Machines T, Hardness K, Machines S, Indenters K, Hardness K, et al. Standard Test Methods for Vickers Hardness and Knoop Hardness of Metallic Materials BT - Standard Test Methods for Vickers Hardness and Knoop Hardness of Metallic Materials 17AD;i:1–27. https://doi.org/10.1520/E0092-17.2.

[37] Cornide J, Garcia-Mateo C, Capdevila C, Caballero FG. An assessment of the contributing factors to the nanoscale structural refinement of advanced bainitic steels. J Alloys Compd 2013;577:S43–7. https://doi.org/10.1016/j.jallcom.2011.11.066.

[38] Rampelberg C, Allain SYP, Geandier G, Teixeira J, Lebel F, Sourmail T. Carbide-free bainite transformations above and below martensite start temperature investigated by in-situ high-energy X-ray diffraction. J Miner Met Mater Soc 2021;73:3181–94. https://doi.org/10.1007/s11837-021-04903-8.

[39] Garcia-Mateo C, Jimenez JA, Yen H-W, Miller MK, Morales-Rivas L, Yang J-R, et al. Experimental evidence on tetragonality of low temperature bainitic ferrite. Int Conf Martensitic Transform (ICOMAT 2014;14.

[40] Jang JH, Bhadeshia HKDH, Suh DW. Solubility of carbon in tetragonal ferrite in equilibrium with austenite. Scr Mater 2013;68:195–8. https://doi.org/10.1016/j.scriptamat.2012.10.017.

[41] Rementeria R, Jimenez JA, Allain SYP, Geandier G, Poplawsky JD, Guo W, et al. Quantitative assessment of carbon allocation anomalies in low temperature bainite. Acta Mater 2017;133:333–45. https://doi.org/10.1016/j.actamat.2017.05.048.

[42] Matsuda H, Mizuno R, Funakawa Y, Seto K, Matsuoka S, Tanaka Y. Effects of auto-tempering behaviour of martensite on mechanical properties of ultra high strength steel sheets. J Alloys Compd 2013;577:S661–7. https://doi.org/10.1016/j.jallcom.2012.04.108.

[43] Hutchinson B, Hagström J, Karlsson O, Lindell D, Tornberg M, Lindberg F, et al. Microstructures and hardness of as-quenched martensites (0.1-0.5%C). Acta Mater 2011;59:5845–58. https://doi.org/10.1016/j.actamat.2011.05.061.

[44] Maruyama N, Tabata S, Kawata H. Excess solute carbon and tetragonality in as-quenched Fe-1Mn-C (C:0.07 to 0.8 mass pct) martensite. Metall Mater Trans A 2020;51:1085–97. https://doi.org/10.1007/s11661-019-05617-y.

[45] Krauss G. Martensite in steel: strength and structure. Mater Sci Eng A 1999;273(275):40–57. https://doi.org/10.1016/S0921-5093(99)00288-9.

[46] Kohne T, Fahlkrans J, Stormvinter A, Maawad E, Winkelmann A, Hedström P, et al. Evolution of martensite tetragonality in high-carbon steels revealed by in situ high-energy X-ray diffraction. Metall Mater Trans A Phys Metall Mater Sci 2023. https://doi.org/10.1007/s11661-022-06948-z.

[47] Hutchinson B, Hagström J, Karlsson O, Lindell D, Tornberg M, Lindberg F, et al. Microstructures and hardness of as-quenched martensites (0.1–0.5%C). Acta Mater 2011;59:5845–58. https://doi.org/10.1016/j.actamat.2011.05.061.

[48] Gaudez S, Teixeira J, Denis S, Geandier G, Allain SYP. Martensite and nanobainite transformations in a low alloyed steel studied by in situ high energy synchrotron diffraction. Mater Char 2022;185:111740. https://doi.org/10.1016/j.matchar.2022.111740.

[49] Kumar A, Singh SB, Ray KK. Influence of bainite/martensite-content on the tensile properties of low carbon dual-phase steels. Mater Sci Eng A 2008;474:270–82. https://doi.org/10.1016/j.msea.2007.05.007.

[50] García De Andrés C, Caballero FG, Capdevila C, Álvarez LF. Application of dilatometric analysis to the study of solid-solid phase transformations in steels. Mater Char 2002;48:101–11.

[51] Verma A, Sundararaman M, Singh JB, Nalawade SA. A new method for determining the Curie temperature using a dilatometer. Meas Sci Technol 2010;21:105106. https://doi.org/10.1088/0957-0233/21/10/105106.

[52] Kurdjumov GV, Khachaturyan AG. Phenomena of carbon atom redistribution in martensite. Metall Trans A 1972;3:1069–76. https://doi.org/10.1007/BF02642438.

[53] Uchima H, Kumagai M, Shimbe J, Tanabe A, Mizuno Y, Onuki Y. Impact of dislocation density and mobility on yielding behavior in quenched medium-carbon martensitic steel tempered at low temperature. ISIJ Int 2022;62. https://doi.org/10.2355/isijinternational.ISIJINT-2021-443. ISIJINT-2021-443.

[54] Takebayashi S, Kunieda T, Yoshinaga N, Ushioda K, Ogata S. Comparison of the dislocation density in martensitic steels evaluated by some X-ray diffraction methods. ISIJ Int 2010;50:875–82. https://doi.org/10.2355/isijinternational.50.875.

[55] Peet MJ, Babu SS, Miller MK, Bhadeshia HKDH. Tempering of low-temperature bainite. Metall Mater Trans A 2017;48:3410–8. https://doi.org/10.1007/s11661-017-4086-x.

[56] Saha Podder A, Bhadeshia HKDH. Thermal stability of austenite retained in bainitic steels. Mater Sci Eng A 2010;527:2121–8. https://doi.org/10.1016/j.msea.2009.11.063.

[57] Saha Podder A. Tempering of a mixture of bainite and retained austenite. University of Cambridge; 2011.

[58] Stone HJ, Peet MJ, Bhadeshia HKDH, Withers PJ, Babu SS, Specht ED. Synchrotron X-ray studies of austenite and bainitic ferrite. Proc R Soc A Math Phys Eng Sci 2008;464:1009–27. https://doi.org/10.1098/rspa.2007.0201.

[59] Garcia-Mateo C, Caballero FG, Miller MK, Jimenez JA. On measurement of carbon content in retained austenite in a nanostructured bainitic steel. J Mater Sci 2012;47:1004–10. https://doi.org/10.1007/s10853-011-5880-2.

[60] Rementeria R, Poplawsky JD, Aranda MM, Guo W, Jimenez JA, Garcia-Mateo C, et al. Carbon concentration measurements by atom probe tomography in the ferritic phase of high-silicon steels. Acta Mater 2017;125:359–68. https://doi.org/10.1016/j.actamat.2016.12.013.

[61] Caballero FG, Miller MK, Clarke AJ, Garcia-Mateo C. Examination of carbon partitioning into austenite during tempering of bainite. Scr Mater 2010;63:442–5. https://doi.org/10.1016/j.scriptamat.2010.04.049.

[62] Caballero FG, Miller MK, Babu SS, Garcia-Mateo C. Atomic scale observations of bainite transformation in a high carbon high silicon steel. Acta Mater 2007;55:381–90. https://doi.org/10.1016/j.actamat.2006.08.033.

[63] Kalish D, Cohen M. Structural changes and strengthening in the strain tempering of martensite. Mater Sci Eng A 1970;6:156–66. https://doi.org/10.1016/0025-5416(70)90045-5.

[64] Hasan HS, Peet MJ, Bhadeshia HKDH. Severe tempering of bainite generated at low transformation temperatures. Int J Mater Res 2012;103:1319–24. https://doi.org/10.3139/146.110788.

[65] Garcia-Mateo C, Peet M, Caballero FG, Bhadeshia HKDH. Tempering of hard mixture of bainitic ferrite and austenite. Mater Sci Technol 2004;20:814–8. https://doi.org/10.1179/026708304225017355.

[66] Wen E, Song R, Xiong W. Effect of tempering temperature on microstructures and wear behavior of a 500 HB grade wear-resistant steel. Metals 2019;9. https://doi.org/10.3390/met9010045.

[67] Couchet C, Allain SYP, Geandier G, Teixeira J, Gaudez S, Macchi J, et al. Recovery of severely deformed ferrite studied by in situ high energy X-ray diffraction. Mater Char 2021;179:111378. https://doi.org/10.1016/j.matchar.2021.111378.

[68] Teramoto S, Imura M, Masuda Y, Ishida T, Ohnuma M, Neishi Y, et al. Influence of iron carbide on mechanical properties in high silicon-added medium-carbon martensitic steels. ISIJ Int 2020;60:182–9. https://doi.org/10.2355/isijinternational.ISIJINT-2019-331.

[69] Podder AS, Lonardelli I, Molinari A, Bhadeshia HKDH. Thermal stability of retained austenite in bainitic steel: an in situ study. Proc R Soc A Math Phys Eng Sci 2011; 467:3141–56. https://doi.org/10.1098/rspa.2011.0212.
[70] Talebi S, Jahazi M, Melkonyan H. Retained austenite decomposition and carbide precipitation during isothermal tempering of a medium-carbon low-alloy bainitic steel. Materials 2018;11:1441. https://doi.org/10.3390/ma11081441.
[71] Totten GE, editor. Steel heat treatment. CRC Press; 2006. https://doi.org/10.1201/NOF0849384523.
[72] Canale LCF, Vatavuk J, Totten GE. Introduction to steel heat treatment. Compr. Mater. Process. 2014:3–37. https://doi.org/10.1016/B978-0-08-096532-1.01202-4. Elsevier.
[73] Horn RM, Ritchie RO. Mechanisms of tempered martensite embrittlement in low alloy steels. Metall Trans A 1978;9:1039–53. https://doi.org/10.1007/BF02652208.